Supplementary Information

Crystallization control via ligand-perovskite coordination for high-performance flexible perovskite solar cells

Xin Chen[†1], Weilun Cai[†1], Tianqi Niu[*1], Hui Wang[2], Chou Liu[1], Zheng Zhang[1], Yachao Du[1], Shuang Wang[1], Yang Cao[1], Pengchi Liu[1], Wenliang Huang[1], Chuang Ma[1], Ben Yang[1], Shengzhong (Frank) Liu,[1,2,3] Kui Zhao[*1]

[1]*Key Laboratory of Applied Surface and Colloid Chemistry, National Ministry of Education; Shaanxi Key Laboratory for Advanced Energy Devices. Shaanxi Engineering Lab for Advanced Energy Technology, School of Materials Science and Engineering, Shaanxi Normal University, Xi'an 710119, P. R. China.*

[2]*Key Laboratory of Photoelectric Conversion and Utilization of Solar Energy, Dalian Institute of Chemical Physics, Chinese Academy of Sciences, Dalian, 116023, Liaoning, China；*

[3]*Center of Materials Science and Optoelectronics Engineering, University of Chinese Academy of Sciences, Beijing, 100049, P. R. China.*

† These authors contributed equally.

** Email: niutq@snnu.edu.cn; zhaok@snnu.edu.cn*

Experimental section

Material preparation **:** Methylammonium chloride (MACl, ≥99.9%), formamidinium iodide (FAI, ≥99.9%), lead iodide (PbI_2, ≥99.99%), and2,2',7,7'-tetrakis(N,N-dimethoxyphenylamine)-9,9'-spirobifluorene (Spiro-OMeTAD) were purchased from Advanced Electron Technology Co., Ltd. Cesium iodide (CsI, 99.9%), Methylammonium iodide (MAI, 99.5%), and 2-Phenylethanamine hydroiodide (PEAI, 99.5%) were brought from Xi'an Polymer Light Technology Corp. Lithium bis(trifluoromethanesulfonyl)imide (Li-TFSI), 4-tert-butylpyridine (tBP, 99.0%), dimethyl sulfoxide (DMSO, 99.9%), N, N-dimethylformamide (DMF, 99.8%), and Tin (IV) oxide (SnO_2) colloidal precursor, 15% in H_2O colloidal dispersion were obtained from Alfa Aesar. Chlorobenzene (CB, 99.8%), isopropanol (IPA, 99.5%), and titanium tetrachloride ($TiCl_4$) were purchased from China National Pharmaceutical Group Corporation.

Device fabrication : The flexible PEN/ITO substrates were ultrasonic cleaned with detergent, deionized water, and ethanol for 30 min each, and then dried by N_2 blowing and treated with ultraviolet-ozone plasma for 10 min. SnO_2 colloidal dispersion was diluted with deionized H_2O in a volume ratio of 1:3 before use. The SnO_2 precursor was spin-coated onto the PEN/ITO substrates at 5000 rpm for 40 s, followed by thermal annealing in air at 120 °C for 45 min. The perovskite solution was prepared by dissolving 783 mg PbI_2, 269 mg FAI, 18 mg CsI, 11 mg MAI, 45 mg MACl, and chlorinated diammonium ligands under different concentrations in 1 mL DMF and DMSO mixture solvent with a volume ratio of 4:1, and stirred for 5 h. For the perovskite deposition process, the perovskite films were deposited using a one-step spin-coating process at 6000 rpm for 30 s. At 20 s before the end of the spin-coating procedure, 900 μL diethyl ether was dropped onto the substrates and then annealed at 120 °C for 15 min. Subsequently, the PEAI solution (5.0 mg/ml in IPA) was dropped on the annealed perovskite films during a spin-coating procedure at 3000 rpm for 30 s. The Spiro-OMeTAD layer was deposited on the top of perovskite films by spin-coating the solution (90 mg Spiro-OMeTAD in 1 mL CB with 22 μL Li-TFSI solution (520 mg in

1 mL ACN), and 36 μL tBP at 5000 rpm for 30 s. Finally, an 80 nm gold electrode was thermally evaporated under vacuum. The construction process of the flexible solar module was carried out as reported in ref. 1.

***Device characterization and theoretical calculations*:** X-ray diffraction (XRD) patterns were measured using a DX-2700BH diffractometer and grazing incidence X-ray diffraction (GIXRD) measurements were conducted using a PANalytical Empyrean diffractometer, which both equipped with Cu Kα radiation. Grazing incidence X-ray scattering (GIWAXs) pattern at an incidence angle of 0.4° was conducted by Shanghai Synchrotron Radiation Facility at the BL17B1 line station. For surface chemical analysis, X-ray photoelectron spectroscopy (XPS) and ultraviolet photoelectron spectroscopy (UPS) were conducted on an ESCALAB 250 photoelectron spectrometer using Al Kα radiation, Thermo Fisher Scientific. UV-visible absorption spectra were recorded using a PerkinElmer UV-Lambda 950 spectrophotometer. Steady-state photoluminescence (PL) spectra and time-resolved photoluminescence (TRPL) spectra were analyzed using a PicoQuant FT-300 spectrometer under an excitation wavelength of 510 nm. *In-situ* PL and UV-vis spectroscopies were described previously as reference 2. Atomic force microscopy (AFM) images were acquired on a Bruker Dimension Icon system. Young's modulus was obtained through a Dimension ICON SPM system. Scanning electron microscopy (SEM) images were measured by a Hitachi SU8020, with a secondary electron detector at an emission current of 10 μA and an accelerating voltage of 3 keV. ToF-SIMS measurement was performed on a PHI nanoTOF II instrument. Electrochemical impedance spectroscopy (EIS) and capacitance-voltage (*C-V*) measurements were performed using an electrochemical workstation (Modulab XM, USA). Current density-voltage (*J-V*) characteristics of F-PSCs were measured by solar simulator equipment (Enlitech, SS-F5) under an illumination intensity of 100 mW cm^{-2} (one sun, AM 1.5G), which was calibrated by a standard silicon cell with a KG5 filter. The non-refractive masks were employed to determine the active device areas of 0.09 and 1.0 cm^2. The dark *J–V* curves were obtained on a Keithley 2400 source meter. The EQE was characterized by the QE-R3011 system (Enli Technology Co., Ltd). The

Vienna ab initio simulation package was applied to perform the DFT calculations under the generalized gradient approximation as the exchange-correlation potential.[3-4] Structure optimization was performed until the force change dropped below 0.03 eV/Å and energy converged to 10^{-5} eV. A kinetic energy cutoff of 500 eV was applied for wave-function expansion and the Γ point was used for electronic Brillouin zone integration.

.

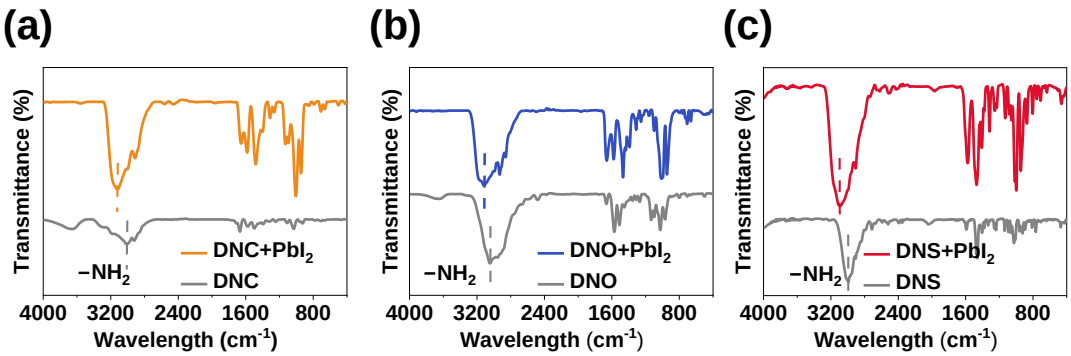

Figure S1. FTIR spectra of neat (a) DNC, (b) DNO and (c) DNS ligands and ligand-PbI_2 films, for which the characteristic peaks of -NH_2 were compared.

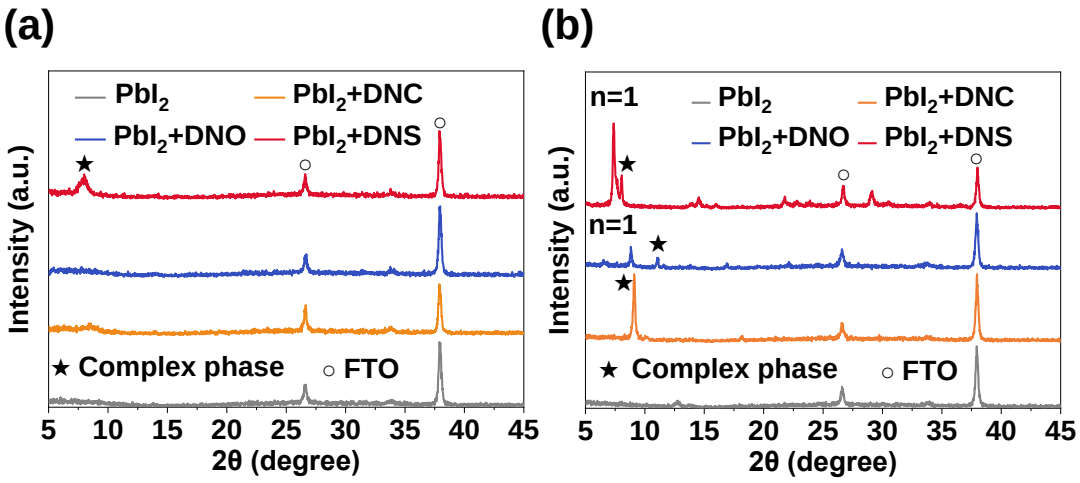

Figure S2. XRD patterns of pristine PbI_2 and ligand-PbI_2 films on FTO substrates before (a) and after (b) thermal annealing. Star and circle marks represent the diffraction signals of ligand-PbI_2 complexes and FTO, respectively.

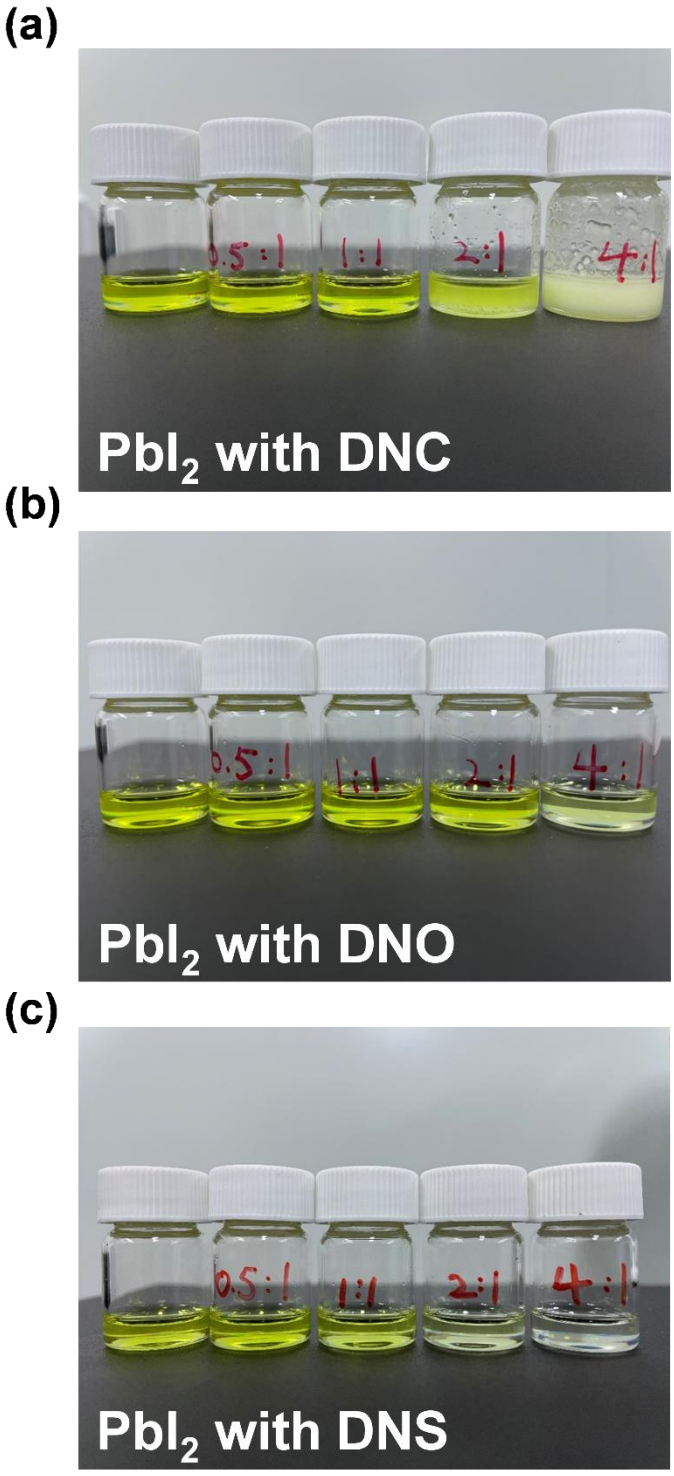

Figure S3. Photographs of PbI_2 solutions with increased incorporation concentration of (a) DNC, (b) DNO and (c) DNS diammonium ligands, showing the color fade along the enlarged molar ratios of ligand:PbI_2.

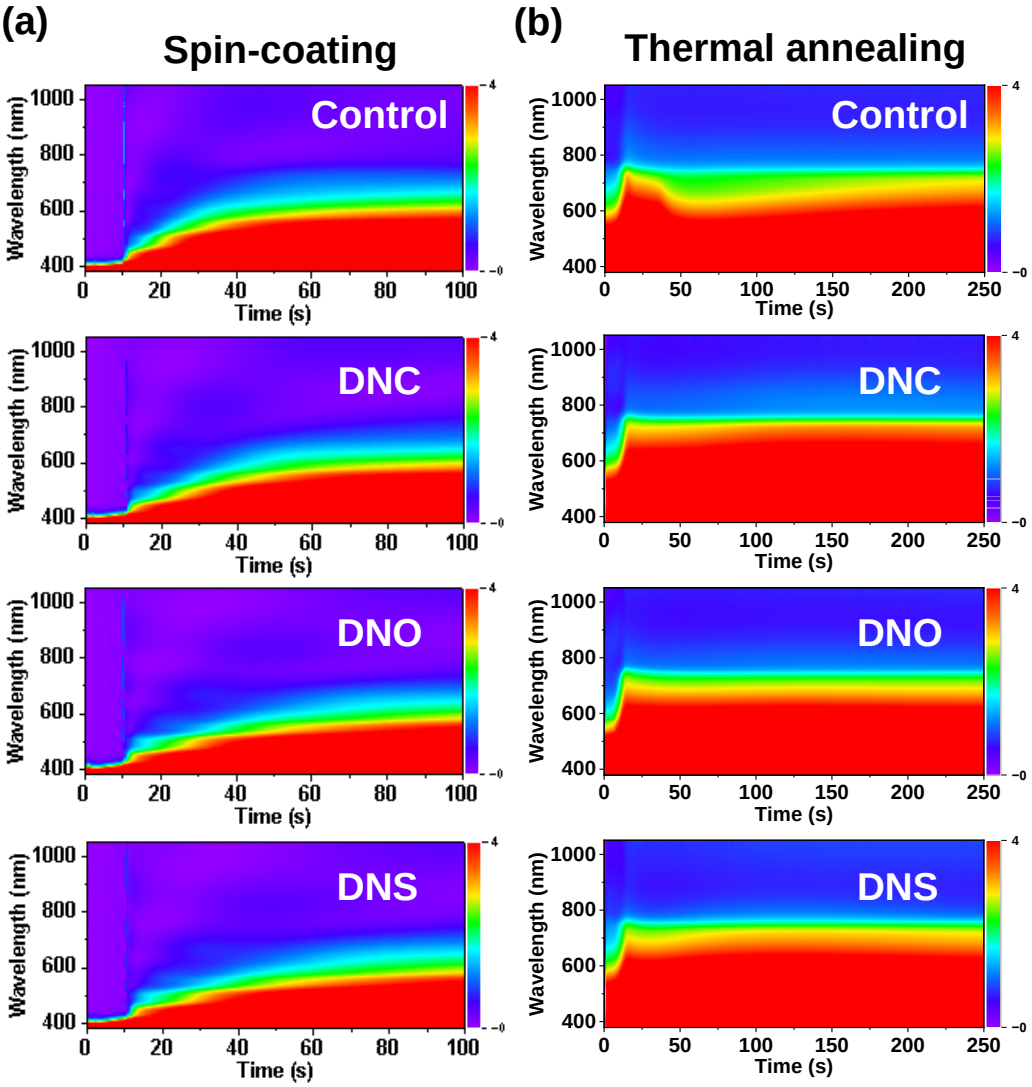

Figure S4. 2D contour maps of *In-situ* UV–Vis spectra of control and ligand-modified films during the (a) spinning-coating and thermal (b) annealing processes.

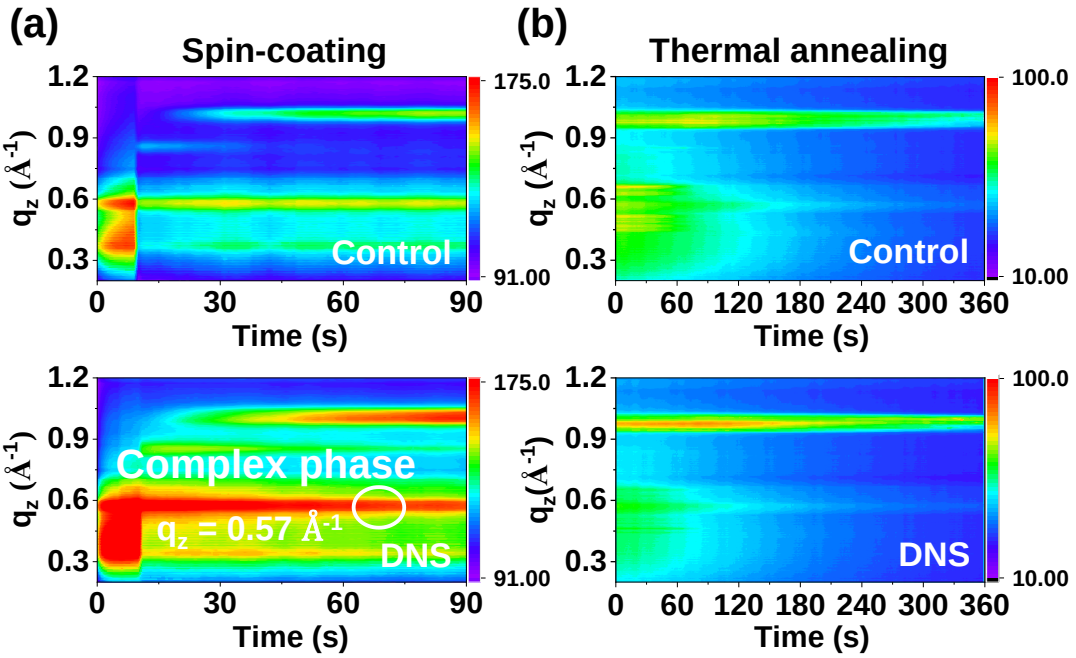

Figure S5. *In situ* GIWAXS measurements of the control and DNS films during the spin-coating (a) and thermal annealing (b). The diffraction signal at q=0.57 Å^{-1} is assigned to the DNS-PbI_2 complex phase.

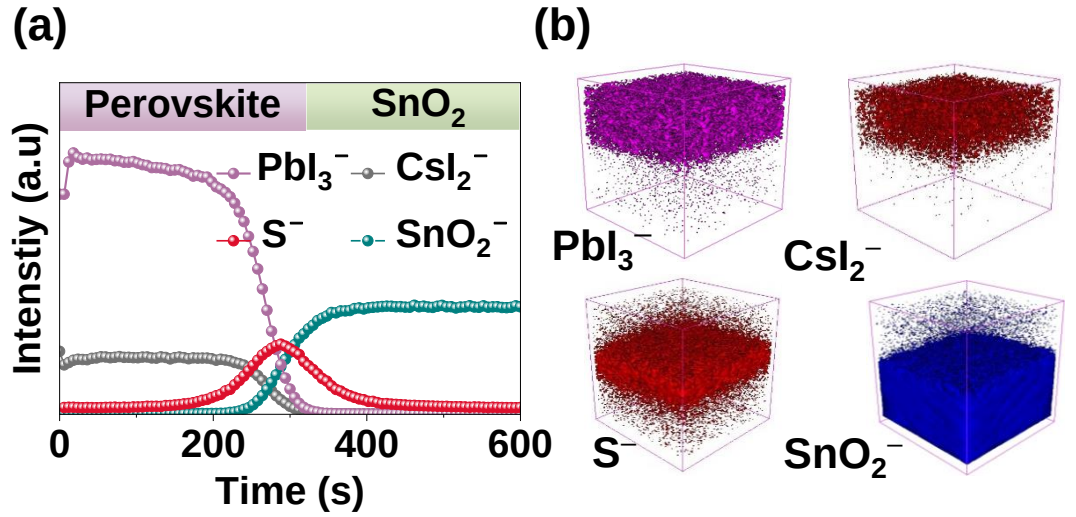

Figure S6. (a) Depth-resolved ToF-SIMS and (b) 3D distribution mapping images of the DNS-based perovskite film on SnO_2/ITO substrate under negative ion mode, showing the dominate distribution of DNS aggregation at the buried interface.

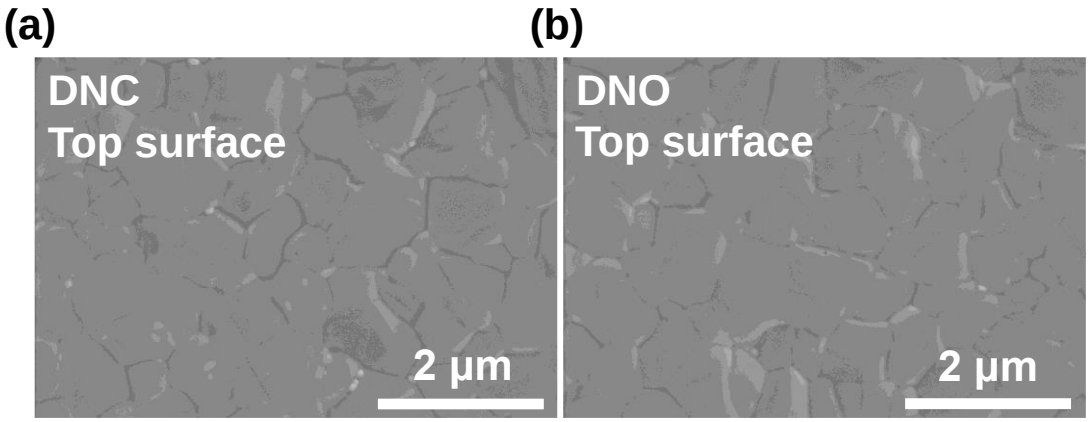

Figure S7. Top-view SEM images of top surface for the (a) DNC and (b) DNO films.

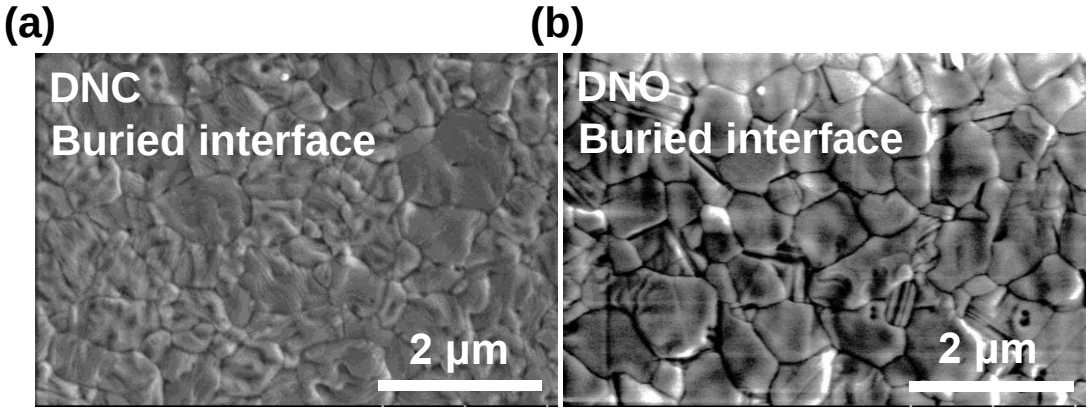

Figure S8. SEM images of (a) DNC and (b) DNO films on bottom interface.

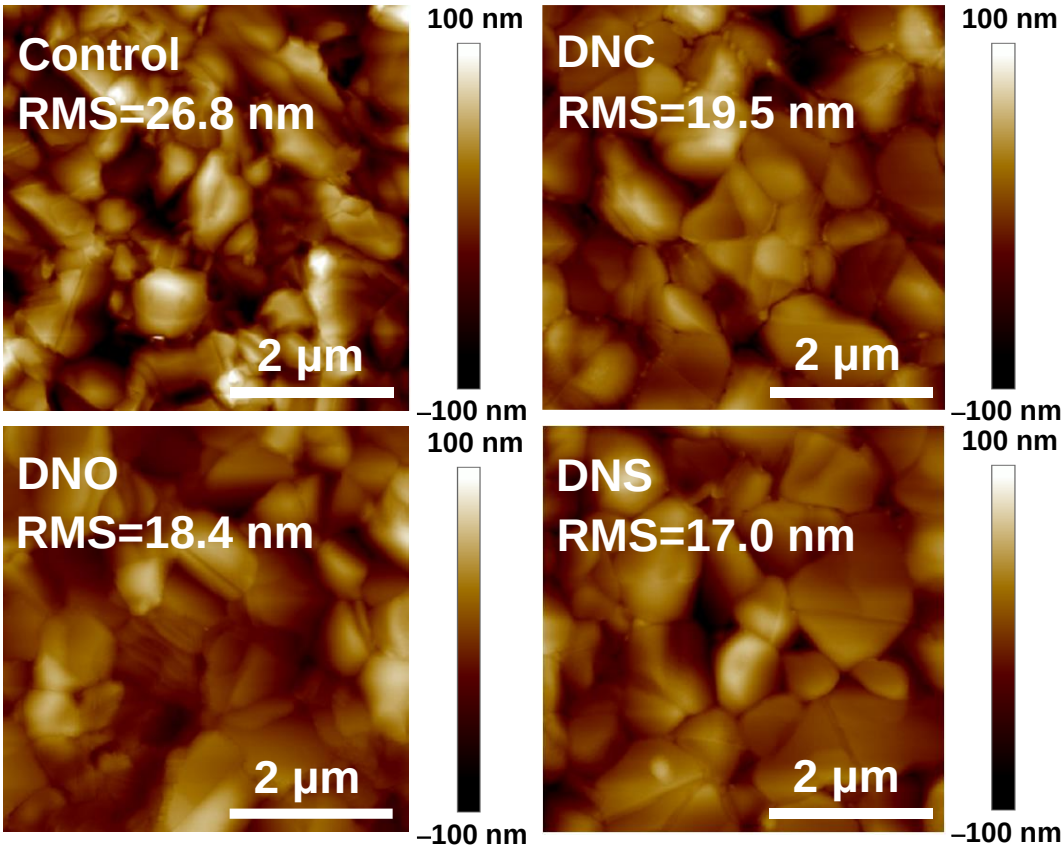

Figure S9. AFM topography images of different perovskite films. showing the root-mean-square roughness (RMS).

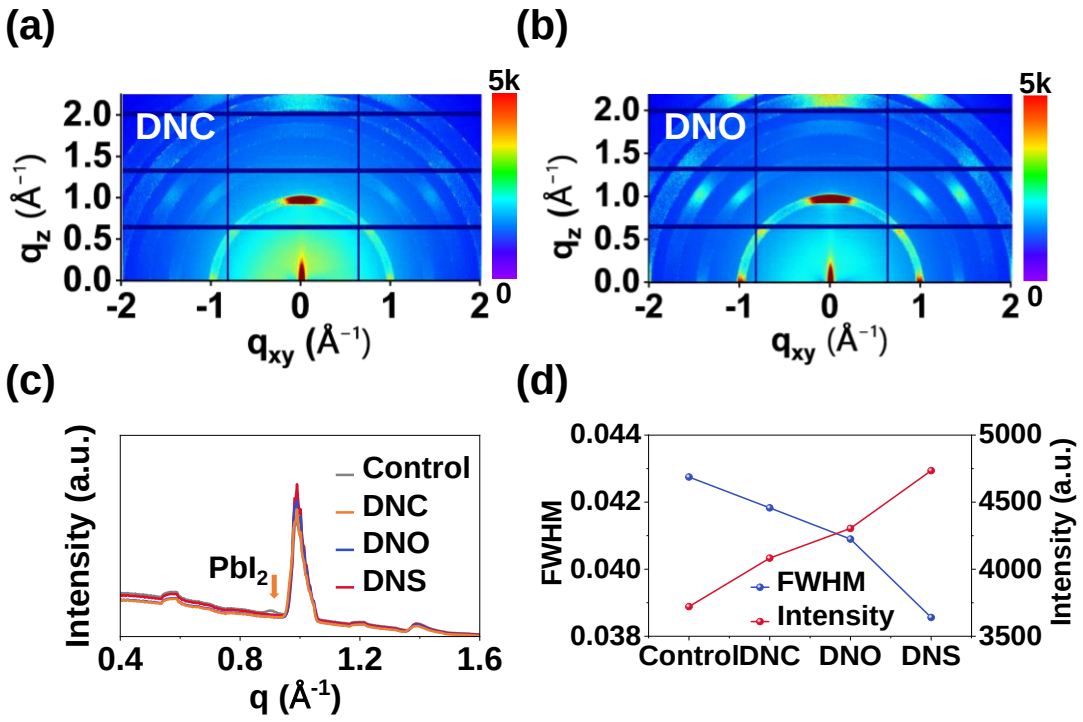

Figure S10. (a-b) The 2D GIWAXs patterns of DNC and DNO films. (c-d) Line-cut profiles (c), full width at half maximum (FWHM) and peak intensity (d) from GIWAXs patterns of different perovskite films.

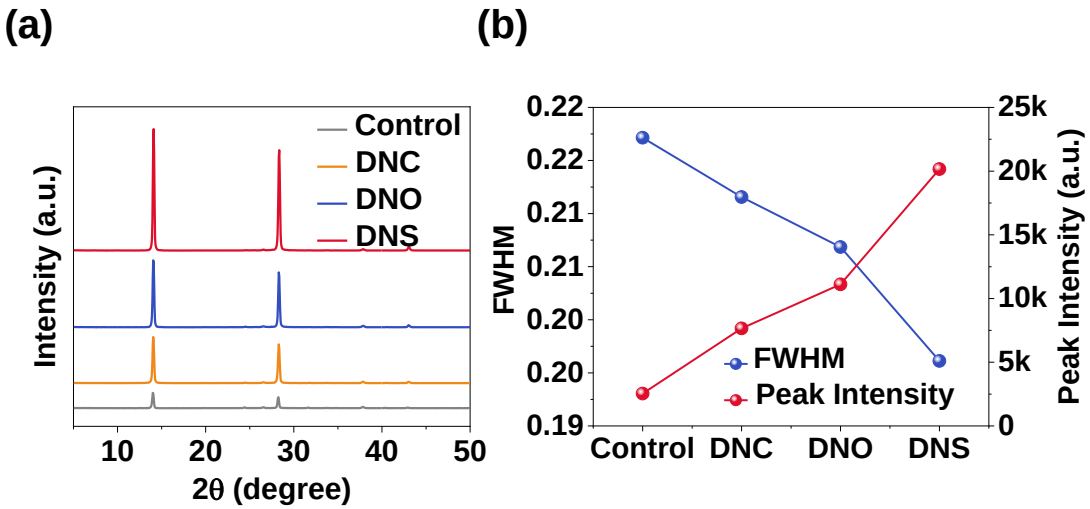

Figure. S11. (a) X-ray diffraction (XRD) patterns and (b) extracted FWHM and peak intensity for different perovskite films.

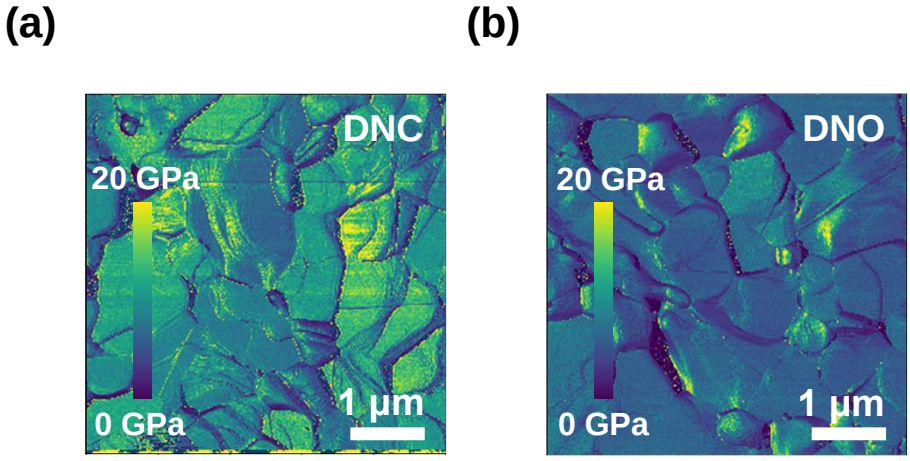

Figure S12. PFQNM images of (a) DNC and (b) DNO films.

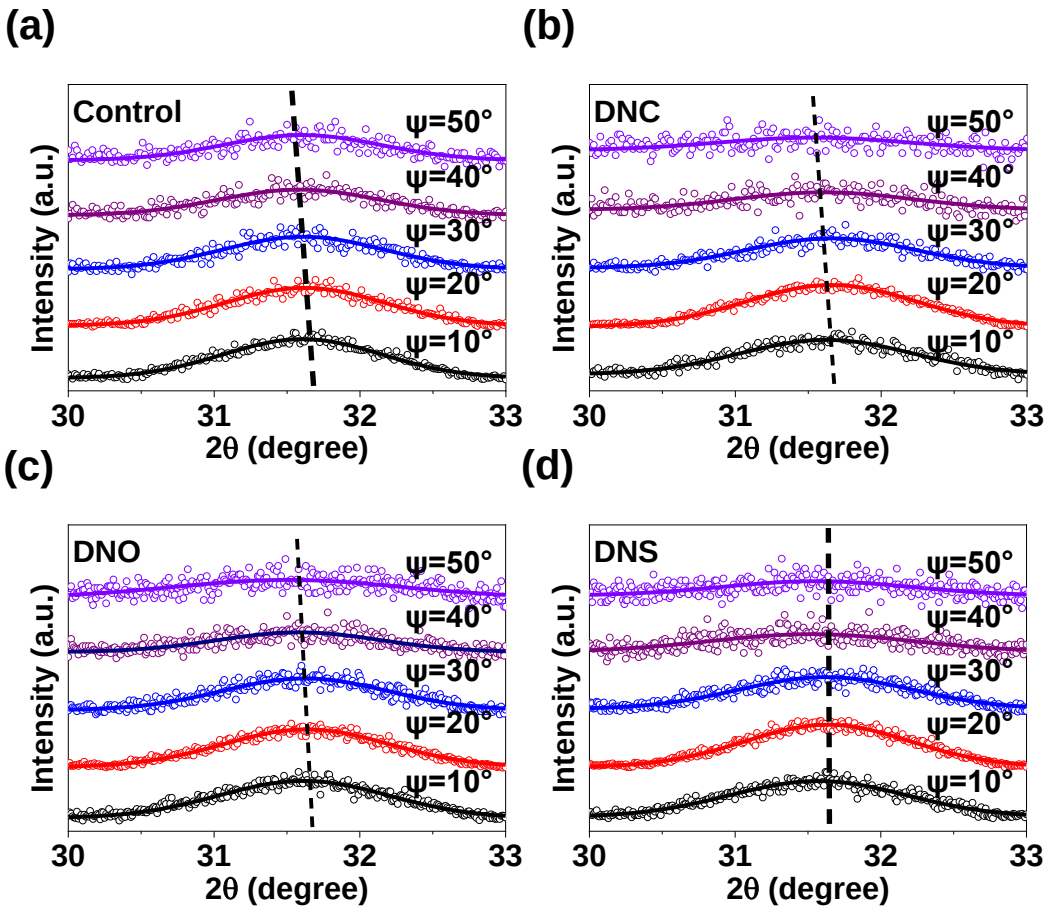

Figure S13. GIXRD spectra at varied ψ angles of the perovskite films using different ligand decorations.

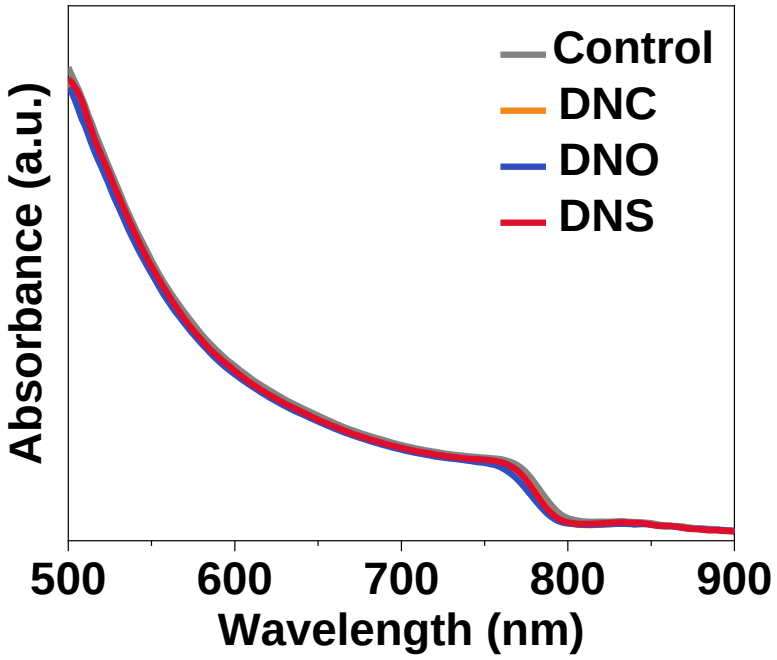

Figure S14. UV-vis absorption spectra of different perovskite films.

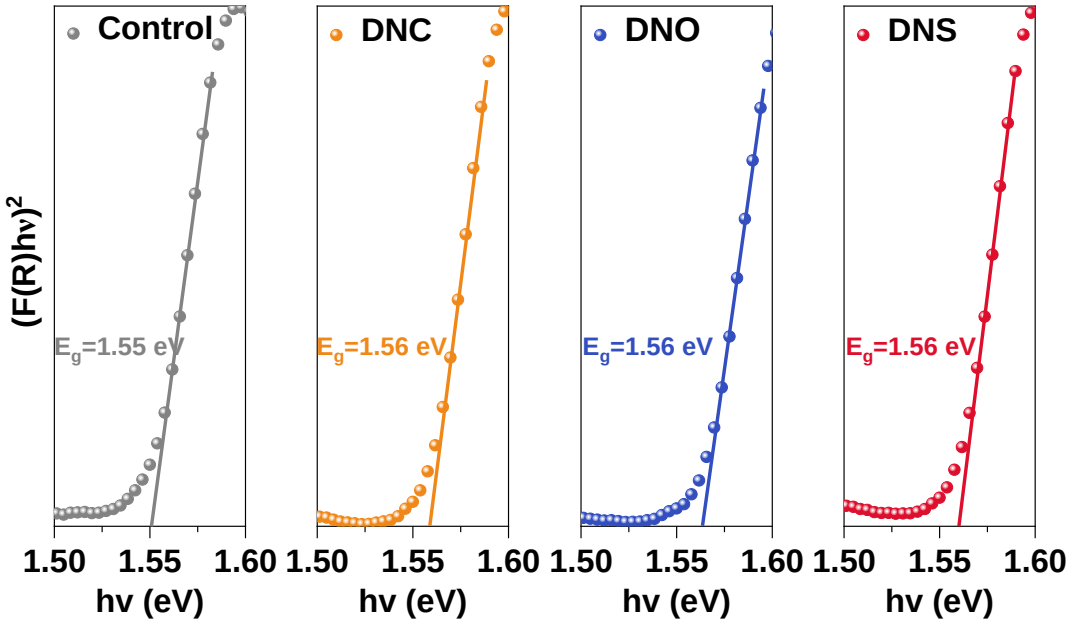

Figure S15. The optical bandgaps derived from the Tauc plots.

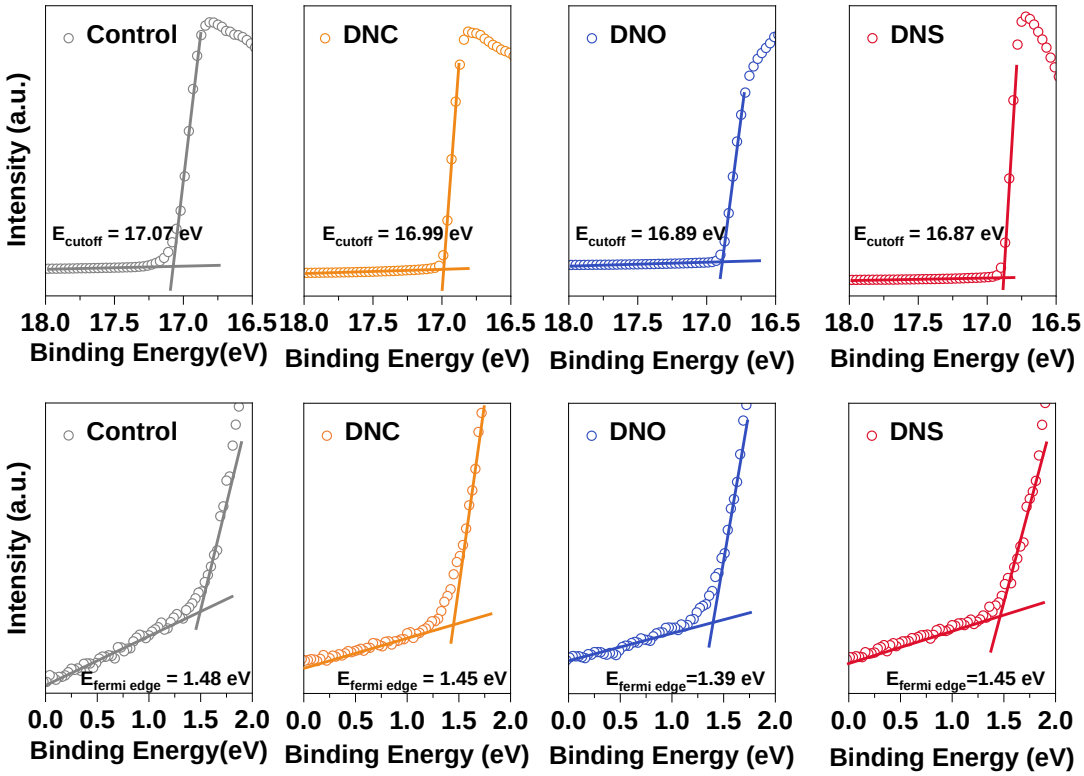

Figure S16. UPS spectra of control and ligand-based perovskite films, determining the E_{cutoff} level and the value of $E_{Fermi\ edge}$ (E_v-E_F).

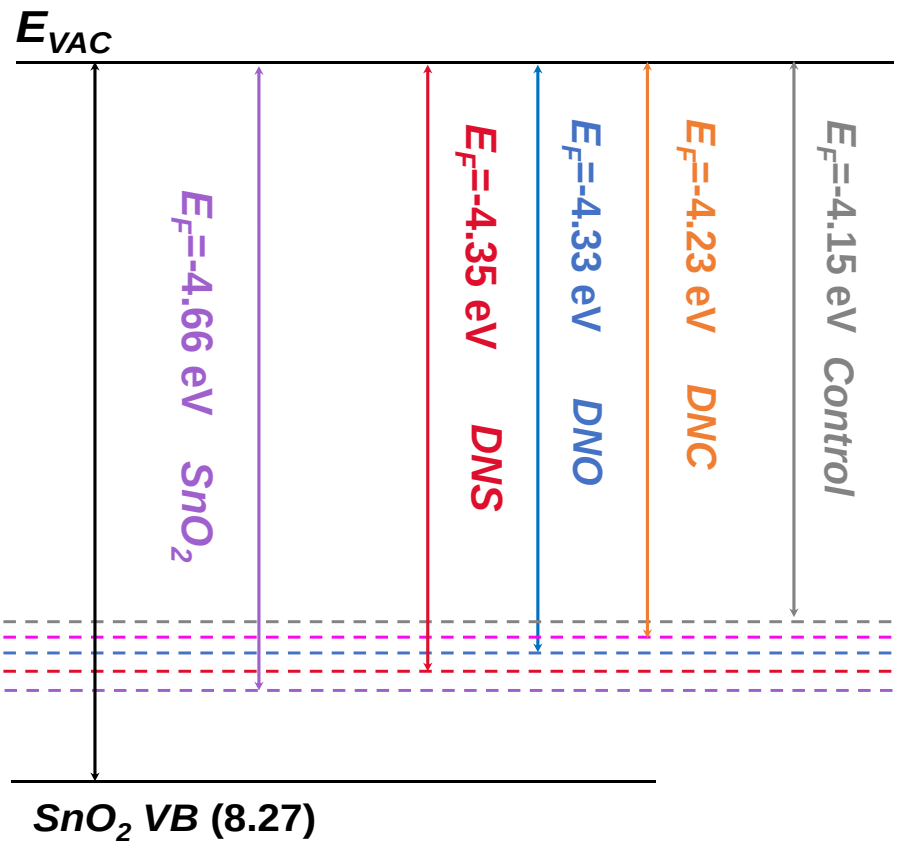

Figure S17. The energy level alignments for different perovskite films with respect to the SnO_2 electron transporting layer.

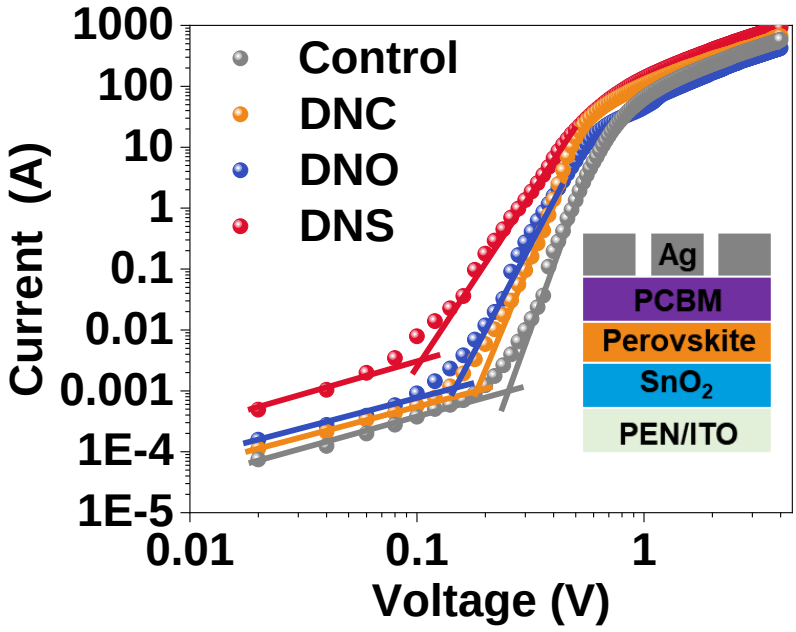

Figure S18. Dark *I-V* curves of the electron-only device (ITO/SnO_2/perovskite/PCBM/Ag), displaying a V_{TFL} kink point behavior.

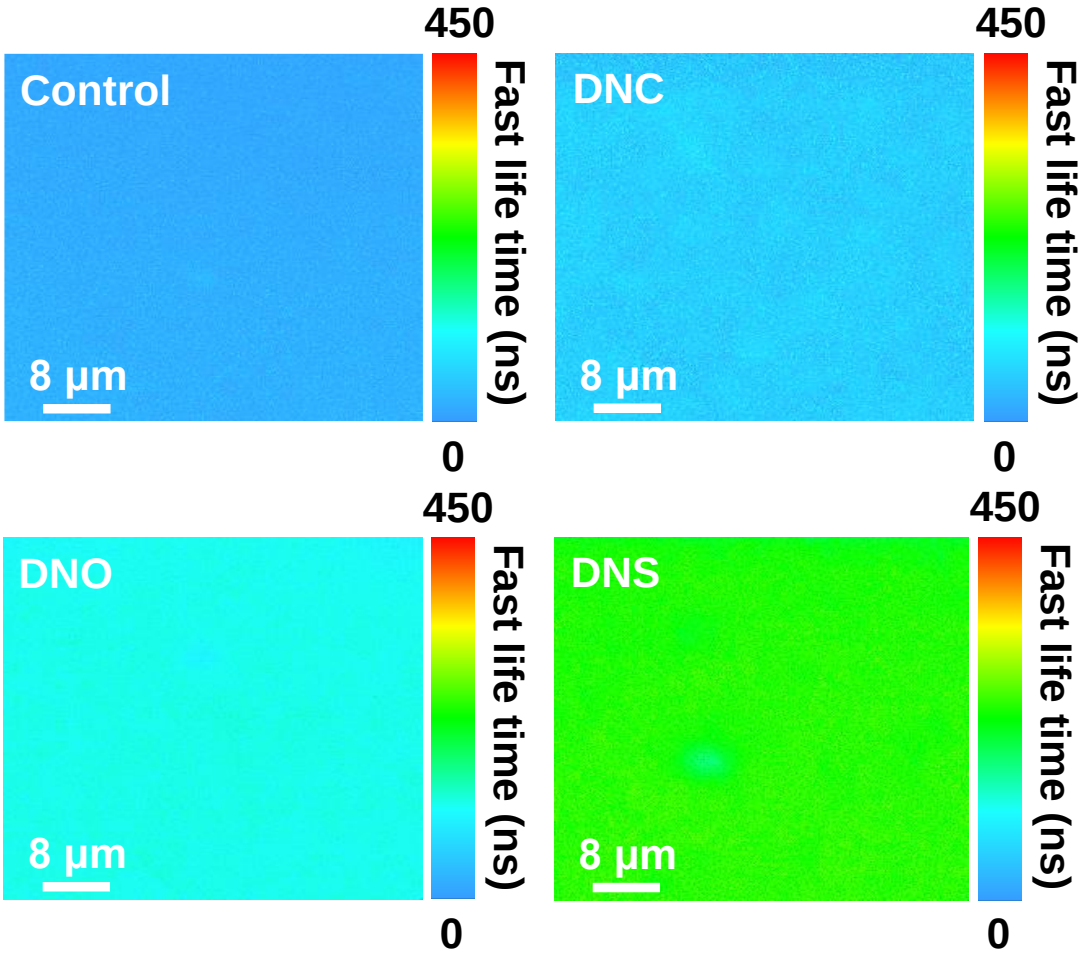

Figure S19. PL lifetime in PL mapping images of the different perovskite films.

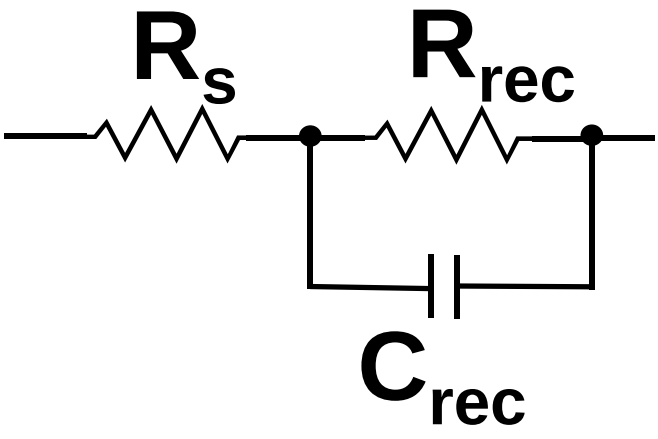

Figure S20. Equivalent circuit composed of the series resistance (R_s) and recombination resistance (R_{rec}).

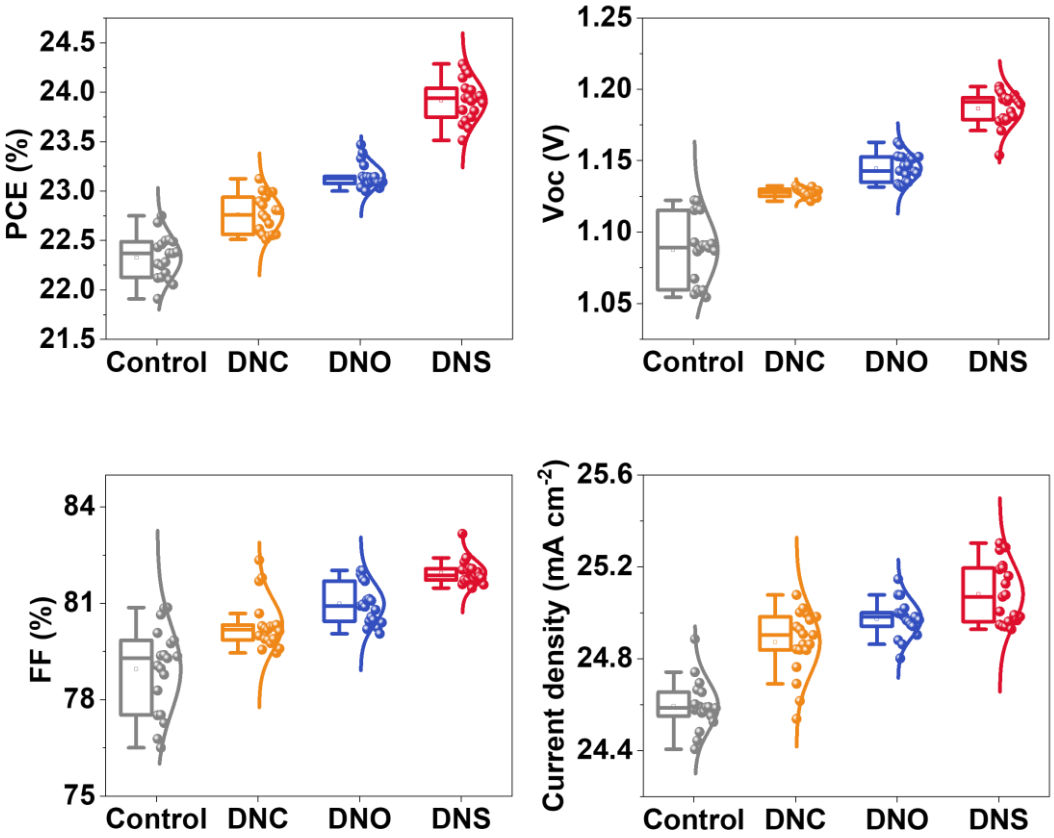

Figure S21. Statistics of photovoltaic parameters for 20 individual devices in each case.

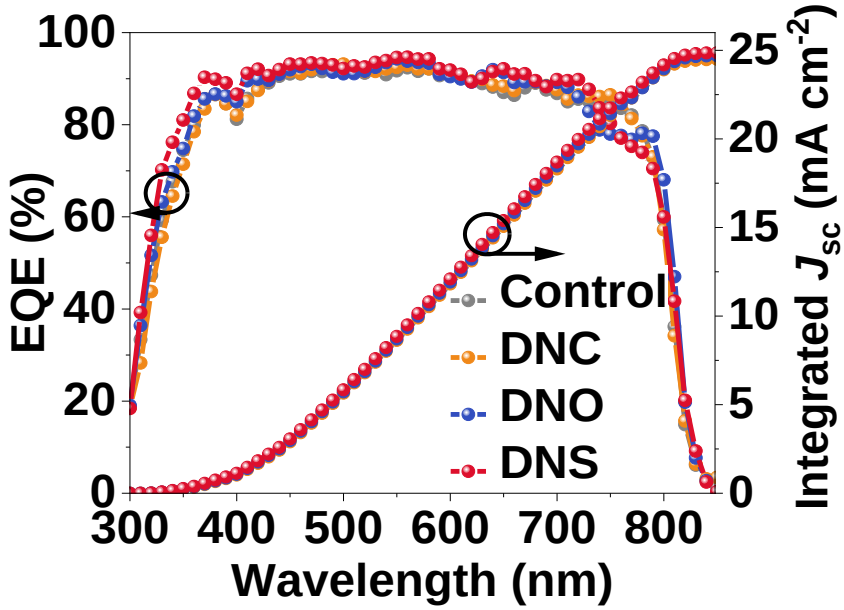

Figure S22. EQE spectra and integrated current density of different F-PSCs.

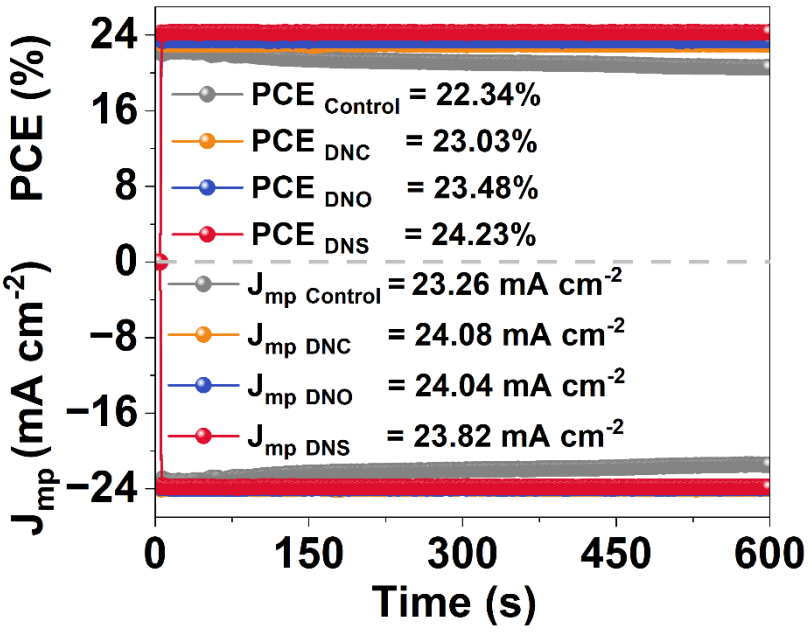

Figure S23. Stabilized power output of the cells measured at a fixed maximum power point (MPP) voltage as a function of time.

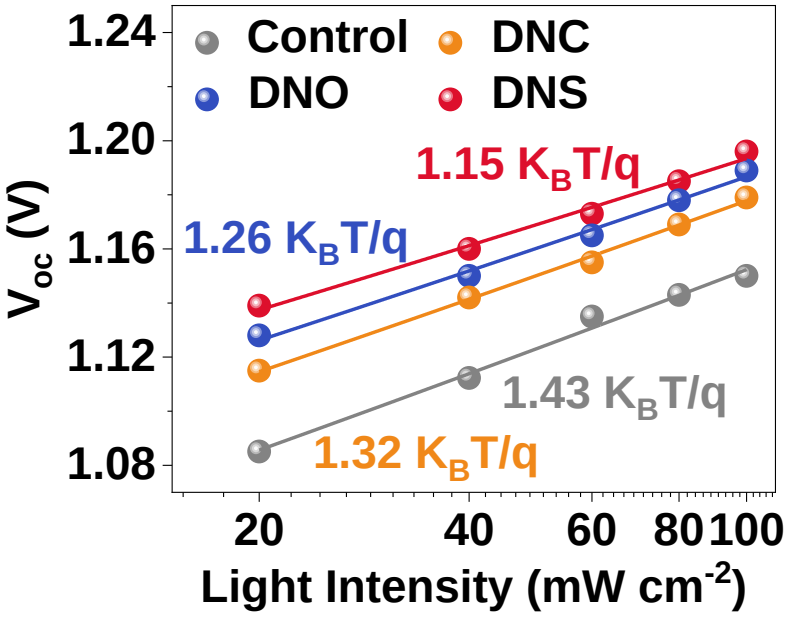

Figure S24. Light intensity-dependent V_{oc} measurements of different F-PSCs.

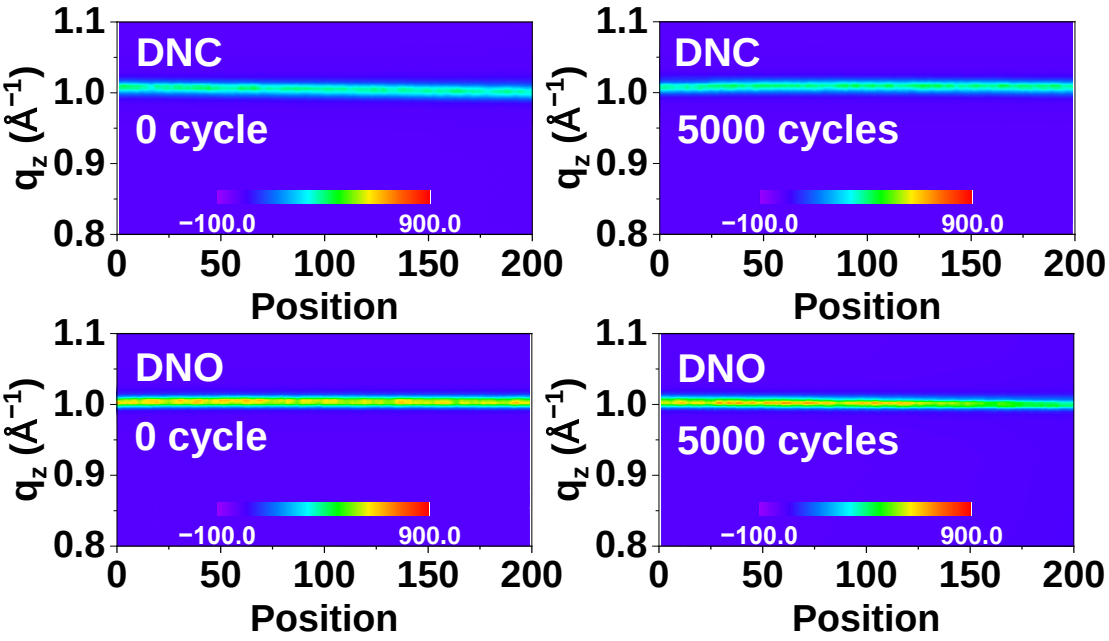

Figure S25. Evolution of GIWAXS patterns of (110) peak for the DNC and DNO films before and after 5000 bending cycles (R=4 mm).

Table S1. Particle size distribution from DLS spectra of different perovskite solutions.

	Control	DNC	DNO	DNS
Diameter (nm)	398.2	474.2	691.7	887.9

Table S2. Fitted parameters of TRPL curves for different perovskite films.

Sample	τ_1 (ns)	A_1 (%)	τ_2 (ns)	A_2 (%)	τ_{ave} (ns)
Control	62.1	58.8	232.4	41.2	185.5
DNC	133.3	47.8	333.5	52.2	279.9
DNO	141.9	30.7	653.6	69.3	608.6
DNS	157.7	30.4	758.5	69.6	708.5

Table S3. Parameters derived from EIS measurements for the different devices.

Sample	R_s (Ω)	C_{rec} (F cm^{-2})	R_{rec} (Ω)
Control	9.6	2.3×10^{-7}	319.2
DNC	8.0	2.7×10^{-7}	1411.0
DNO	6.3	8.8×10^{-7}	1843.1
DNS	5.9	7.6×10^{-7}	2710.4

Table S4. Photovoltaic parameters of champion F-PSCs with an active area of 0.09 cm².

Sample	V_{oc} (V)	FF (%)	J_{sc} (mA cm^{-2})	PCE (%)
Control	1.12	80.8	24.73	22.51
DNC	1.16	81.0	24.75	23.31
DNO	1.17	81.7	24.76	23.82
DNS	1.18	82.4	25.18	24.47

Table S5. Photovoltaic parameters of champion F-PSCs with an active area of 1.0 cm².

Sample	V_{oc} (V)	FF (%)	J_{sc} (mA cm^{-2})	PCE (%)
Control	1.08	74.7	24.69	20.08
DNC	1.09	77.4	24.74	20.97
DNO	1.12	80.5	24.80	22.39
DNS	1.13	82.2	24.85	23.16

Table S6. Photovoltaic parameters of flexible solar module on a 19.8 cm² scale.

V_{oc} (V)	FF (%)	I (mA)	PCE (%)	Pmax (mW)	Ps (W kg^{-1})
11.15	76.1	40.52	17.21	344.10	1491.8

References

1. Yang, D.; Yang, R.; Zhang, C.; Ye, T.; Wang, K.; Hou, Y.; Zheng, L.; Priya, S.; Liu, S., Highest-Efficiency Flexible Perovskite Solar Module by Interface Engineering for Efficient Charge-Transfer. *Adv. Mater.* **2023,** *35*, 2302484.

2. Wang, S.; Yang, T.; Yang, Y.; Du, Y.; Huang, W.; Cheng, L.; Li, H.; Wang, P.; Wang, Y.; Zhang, Y.; Ma, C.; Liu, P.; Zhao, G.; Ding, Z.; Liu, S.; Zhao, K., In Situ Self-Elimination of Defects via Controlled Perovskite Crystallization Dynamics for High-Performance Solar Cells. *Adv. Mater.* **2023,** *35*, 2305314.

3. Perdew, J. P.; Burke, K.; Ernzerhof, M., Generalized Gradient Approximation Made Simple. *Phys. Rev. Lett.* **1996,** *77*, 3865-3868.

4. Kresse, G.; Joubert, D., From ultrasoft pseudopotentials to the projector augmented-wave method. *Phys. Rev. B* **1999,** *59*, 1758-1775.